PtSe(2)outperforms Pt as a counter electrode in dye sensitized solar cells

G. Syrrokostas, K. Bhorkar, L. Sygellou, V. Dracopoulos, G. Leftheriotis, S.N. Yannopoulos

CRediT author statement

Syrrokostas George: Conceptualization, Investigation, Writing- Original draft preparation, Writing - Review & Editing ,Visualization, Funding acquisition. **Bhorkar Kapil:** Conceptualization, Methodology, Validation, Investigation, Writing - Review & Editing. **Sygellou Labrini:** Investigation, Formal Analysis. **Dracopoulos Vasilis:** Investigation. **Leftheriotis George:** Resources, Writing - Review & Editing. **Yannopoulos Spyros N.:** Writing - Review & Editing, Supervision, Funding acquisition

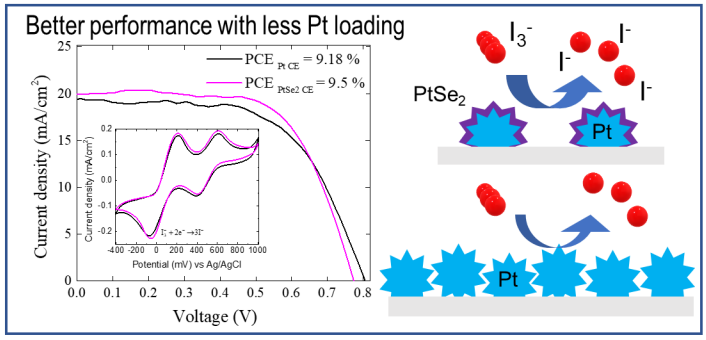

$PtSe_2$ outperforms Pt as a counter electrode in Dye Sensitized Solar Cells

G. Syrrokostas,[1,2,*] K. Bhorkar,[1,3] L. Sygellou,[1] V. Dracopoulos,[1] G. Leftheriotis,[2] and S.N. Yannopoulos[1,*]

[1] *Foundation for Research and Technology Hellas – Institute of Chemical Engineering Sciences (FORTH/ICE-HT), P.O. Box 1414, GR-26504, Rio-Patras, Greece*

[2]*Department of Physics, University of Patras, GR-26504, Rio-Patras, Greece*

[3]*Univ. of Rennes, CNRS, ISCR – UMR 6226, F-35000 Rennes, France*

[#]Corresponding Author:

Dr. George Syrrokostas
Department of Physics, University of Patras, GR-26504, Rio-Patras, Greece
Phone: +30 2610 997 431,
E-mail: gesirrokos@upatras.gr

Dr. Spyros N. Yannopoulos
FORTH/ICE–HT, P.O. Box 1414, GR-26504, Rio-Patras, Greece
Phone: +30 2610 965 252,
E-mail: sny@iceht.forth.gr

Abstract

In the present study, we show that $PtSe_2$ films, prepared by soft selenization of pre-deposited Pt, is a very efficient counter electrode (CE) in dye sensitized solar cells (DSSCs). Devices based on $PtSe_2$ achieve better photoconversion efficiency (9.5 ± 1.2 %) than those employing bare Pt CE (9.18 ± 0.21 %), even if the latter use three times more Pt loading than that used to prepare the $PtSe_2$ CE. Films with of various Pt loadings have been prepared by electrodeposition and their catalytic properties have been investigated and compared with films of corresponding Pt loading which have been transformed to $PtSe_2$ by low-temperature selenization. The improved performance of the $PtSe_2$ CEs has been assigned to the higher availability of catalytic active sites and the more effective mechanism of interfacial electron transfer. This is a first attempt to explore the role of $PtSe_2$ as the CE in DSSCs. The strong advantages of $PtSe_2$ in relation to catalytic activity, stability, efficiency, combined with cost reduction, due to the lower mass loading required for a given performance, renders this noble-transition metal dichalcogenide a promising candidate to boost the performance of third generation photovoltaics, opening-up possibilities, at the same time, for other applications where Pt is used as the catalyst.

Keywords: counter electrode, platinum diselenide, dye sensitized solar cells, electrodeposition, low temperature selenization.

1. Introduction

Solar photovoltaics, along with other renewable energy technologies, provide a means to produce electrical energy in a sustainable manner. Currently, the technology of solar photovoltaics has reached its third-generation, which includes dye-sensitized solar cells (DSSCs), organic (OPVs) and perovskite solar cells (PSCs), promising even lower materials and production costs, a wider range of applications and comparable performance with Si-based photovoltaics [1–6].

DSSCs have been widely investigated both in the lab and for large-scale applications [7,8]. A typical DSSC consists of a dye-sensitized photoanode, an electrolyte containing a redox couple (e.g. I^-/I_3^-), and a counter electrode (CE). At the CE, a catalyst, Pt, layer is commonly used, deposited on a conductive substrate (commonly transparent conductive oxides (TCO), such as FTO and ITO). This serves to minimize the charge transfer resistance (R_{CT}), ensuring a high exchange current density for the reduction of the oxidized species of the electrolyte. A value of 2-3 Ω cm^2 is desirable for R_{CT} [9], while electrical conductivity, mechanical and electrochemical stability [9], are also needed for a high-performance CE. Different approaches have been proposed for improving the catalytic properties (surface area, activity) [10–12] and stability of Pt-based CEs, to tackle particular issues such as Pt detachment from TCO and formation of PtI_4 [10,13].

As an alternative to Pt, other metals, carbon-based materials, conductive polymers, transition metal chalcogenides and complex alloys are as well explored as CEs [9,10,14] and a few recent review articles appear in the relevant literature [15–18]. In particular, transition metal selenides and alloys with the general formula of M_xSe_y, where M is a transition metal from groups 5-10, have been already evaluated as CEs in DSSCs [19] [20] (Table S1 and Fig. S1), due

to their distinctive electronic and chemical properties. Exhibiting higher optical transparency and charge transfer ability, in comparison to Pt, transition metal selenides are ideal candidates for bifacial DSSCs [21–23] or for photoelectrochromic devices [24]. Besides, intentional defect formation, offers additional active sites for I_3^- adsorption and reduction [25]. For example, Sun *et al.* used single-crystal $CoSe_2$ nanorods as an efficient electrocatalyst for CE in a DSSC replacing Pt, and achieved an increase in the photoconversion efficiency (PCE) value from 8.17% to 10.2% [26]. CoSe hollow spheres [27] exhibited excellent electrocatalytic activity along with a light-scattering ability, resulting in PCE of ~10.35%, compared to ~8.57% for the bare Pt CE. Similar improvements were also observed in several works, [25,28–30], where an iodide/triiodide redox couple was used, whereas the electrocatalytic properties of $CoSe_2$ CEs against a cobalt ($2^+/3^+$) redox couple were also examined in [21,29]. Using a transparent $Co_{0.85}Se$/graphene composite film as a CE, a PCE of 11.26% was achieved, compared to 9.68% for the Pt CE [21].

CEs with group 5 diselenides (MSe_2, M=V, Nb, Ta), such as VSe_2 with a cauliflower-like morphology [31] and $NbSe_2$ nanosheets [32], both showing a metallic behavior, have outperformed Pt-based CEs, while $TaSe_2$ exhibited as a CE inferior performance compared to Pt [33]. In the same work, group 6 selenides ($MoSe_2$, WSe_2) were also prepared via a solvothermal method, where WSe_2 showed the best electrocatalytic properties among the other selenides, due to the lower charge transfer resistance at the CE/electrolyte interface; however, PCEs were inferior to the efficiency of the Pt CE [33] (Figure S1). However, a CE based on few-layered $MoSe_2$ nanostructures, fabricated by surface selenization of a molybdenum coated glass, surpassed the PCE achieved by a Pt-based CE [34]. Group 8 diselenides (MSe_2, M=Fe, Ru) have been also evaluated as CEs. Recently, a $FeSe_2$ CE showed not only an improved PCE (7.2%) compared with a Pt CE (6.99%), but also enhanced corrosion resistance to the I^-/I_3^- redox

electrolyte [35]. Moreover, a few binary-alloy metal selenides (M-Se: M=Co, Ni, Cu, Fe, Ru) were applied as CEs in bifacial DSSCs in [25], exhibiting transparencies higher than 70% in the visible and NIR and a PCE value up to 9.22% in the case of a $Ru_{0.33}Se$ CE, compared to 7.23% for a Pt CE.

Notably, from group 10 selenides (MSe_2, M=Ni, Pd, Pt) only nickel-based compounds have been evaluated as CEs in DSSCs. Wu *et al.* [36] examined the effect of the morphology of NiSe CEs on their electrochemical activity and stability, and on the PCE of the resulting DSSCs. In the case of nanoparticles, the PCE value (7.82%) surpassed that of a Pt CE (7.62%) [36]. Similarly, a transparent $Ni_{0.85}Se$ CE yielded a PCE of 10.63% compared with 8.78% for a Pt CE, when they were irradiated from both sides [23], while a ternary alloy of $NiCoSe_2$ showed an enhanced catalytic activity towards the iodide/triiodide redox couple, resulting in an improvement in PCE value of corresponding DSSCs, compared with bare Pt [37]. Other efforts for substituting Pt with NiSe were not so successful [28,35]. Based on this brief survey, it is evident that there are no reports so far studying the CE performance of two important members of group 10 selenides, namely $PtSe_2$ and $PdSe_2$ in DSSCs.

The above findings have been the incentive to explore the efficiency of an emerging 2D layered material, namely platinum diselenide ($PtSe_2$), as an alternative CE for DSSCs. $PtSe_2$ exhibits high carrier mobility, a semi-metallic or a semiconducting behavior with a layer dependent optical band gap [38]. This material has been explored as a gas sensor, in opto-electronic devices and in catalysis [39–41]. A recent study on the vertical heterostructure of $PtSe_2$ with 1D-Sb_2Se_3 demonstrates type-II heterojunction that can serve as a self-powered broadband photodetector for the visible-NIR region [42]. Up to now, the electrocatalytic activity of $PtSe_2$ has been examined only for the hydrogen evolution reaction (HER). In that case, a variety of parameters have been examined for optimizing the HER activity, such as the density of

the active sites on the edges or on the basal plane [43,44], the number of layers [45,46] and its crystal structure [47], whereas an electrochemical reduction was used for improving the HER activity of layered Pt dichalcogenides [48]. However, in all cases, the HER catalytic performance was found to be inferior to that of bare Pt or Pt/C electrodes.

To sum up, transition metal selenides (M_xSe_y) are promising candidates for efficient CEs in DSSCs, due to their comparable or even better, in some cases, electrocatalytic properties compared to Pt, having though a lower cost. Among the different M_xSe_y, a group 10 selenide, namely $PtSe_2$, was explored in the current work for the first time as a CE in DSSCs and compared with equivalent bare Pt CEs. As a result, a more rational utilization of the expensive and scarce Pt metal was achieved using $PtSe_2$ as CE, improving further the cost-performance ratio of DSSCs.

2. Experimental

2.1 Deposition of platinum and $PtSe_2$ formation

Platinum films were prepared by electrodeposition, at a constant potential of −400 mV applied using an Autolab PGSTAT 204 potentiostat, for different time intervals ranging from 50 s to 400 s. An aqueous hexachloroplatinic acid solution (0.002 M) and a three-electrode configuration were used, with a bare FTO glass substrate (15 Ω/sq) serving as the working electrode, an Ag/AgCl electrode as the reference and a Pt wire as the counter electrode [12,49]. The samples prepared in this study are denoted as Pt-50, Pt-100, Pt-200 and Pt-400, which correspond to the Pt electrodeposition times of 50, 100, 200, and 400 s, respectively.

Low-temperature selenization was used to convert the electrodeposited Pt films into $PtSe_2$. The selenization step took place in a tube furnace at 430 ^oC for 90 min, under the flow of Ar gas

at a flow rate of 100 sccm. Pellets of ultrapure Se (Alfa Aesar, purity 99.9990%) were placed upstream at ~220 ^{o}C to provide adequate vapor pressure in the tube. Based on the notation provided above, the selenized films will be denoted as sPt-50, sPt-100, sPt-200, and sPt-400.

2.2 Characterization of Pt and $PtSe_2$ films

Electron microscopy images for characterizing the morphologies of the prepared Pt films, before and after selenization, were recorded by a high-resolution field-emission scanning electron microscope (FE-SEM) instrument (Zeiss, SUPRA 35VP) operating at 15 kV. The Raman spectra were excited using an Ar ion laser (514.5 nm). A micro-Raman set-up (T-64000, Jobin-Yvon, France) was employed to analyse backscattered light which was focused by an objective to an area of 2–3 μm. The Raman mode of Si single crystal at 520 cm^{-1} was used to calibrate the wavenumber scale of the spectra. Low incident laser power was used to avoid heat-induced damage of the crystals.

The surface analysis measurements were performed in a UHV chamber (P~5×10^{-10} mbar) equipped with a SPECS Phoibos 100-1D-DLD hemispherical electron analyzer and a non-monochromatized dual-anode Mg/Al x-ray source for XPS. The XP spectra were recorded with MgKa at 1253.6 eV photon energy and an analyzer pass energy of 15 eV giving a Full Width at Half Maximum (FWHM) of 0.85 eV for $Ag3d_{5/2}$ line. The analyzed area was a spot of 3 mm in diameter. The atomic ratios were calculated using the intensity (peak area) of the XPS peaks weighted with the corresponding relative sensitivity factors (RSF) and the energy analyzer transmission function. For spectra collection and treatment, including fitting, the commercial software SpecsLab Prodigy (by Specs GmbH, Berlin) was used. The XPS peaks were

deconvoluted with a sum of Gaussian-Lorentzian peaks after a Shirley type background subtraction.

Cyclic voltammetry (CV) was used to evaluate the catalytic activity of Pt and $PtSe_2$ electrodes towards the iodide/triiodide (I^-/I_3^-) redox shuttle. The composition of the electrolyte, used for the CV experiments was 10 mM KI, 1 mM I_2 and 0.1 M $LiCLO_4$ in propylene carbonate. The same three-electrode setup was used as in the case of the electrodeposition of Pt described above, with the sweep rate varying between 5 and 60 mV s^{-1}. Moreover, the electrochemical stability of the platinum-based films was evaluated by performing continuous cycling (up to 100 cycles).

Symmetric dummy cells with two identical electrodes were prepared for performing Tafel and EIS analysis. The cells were sealed using a thermoplastic sealant (Surlyn, GreatCellSolar, 50 μm thickness) at 120 ^oC for 10 min and the same liquid redox electrolyte as in the case of DSSCs (see below) was used. Tafel polarization curves were recorded from 1 to -1 V with a scan rate of 100 mV/s. The EIS spectra were recorded using a frequency range from 5 kHz to 0.1 Hz, while the ac amplitude was 10 mV at open circuit. The Nova 1.10 software was used for the analysis.

2.3 Fabrication and performance study of dye-sensitized solar cells

Nanostructured TiO_2 films were deposited on an FTO/glass substrate (15 Ω/sq) by the doctor blade method, using a glass slide, after preparing an appropriate paste according to our previous work [50]. After air drying, TiO_2 films were annealed at 450 ^oC for 30 min. Their thickness (~10 μm) was measured using an Ambios XP-1 stylus profilometer. Sensitization was performed by soaking the TiO_2 films, while being heated at 80 ^oC, overnight in a N719 dye solution (0.3 mM in EtOH). The sensitized TiO_2 films and the Pt or $PtSe_2$ films, serving as counter electrodes, were arranged to face each other. Sealing was performed by placing the

electrodes at 120 ^{o}C for 10 min, using a thermoplastic sealant (Surlyn, GreatCellSolar, 50μm thickness). Finally, a liquid redox electrolyte, supplied also by GreatSellSolar (EL-HPE High Performance Electrolyte), was inserted from tiny holes pre-drilled at the counter electrode. The holes were then sealed with Surlyn and a small piece of glass.

An Oriel 96000 solar simulator, equipped with an AM1.5G filter, in conjunction with a Keithley 236 source meter was used for recording the characteristic J-V curves of the DSSCs. The incident irradiance was fixed at nearly 1000 W/m^2 [50], as measured using a calibrated photodiode before each measurement.

3. Results

3.1 Effect of electrodeposition time on film morphology

A typical variation of the current density during a potentiostatic electrodeposition procedure ($V_{applied}$ = - 400 mV) is shown in Fig. S2a. The observed variation is explained by a progressive nucleation mechanism, as proposed elsewhere [51]. Pt loading or equally the amount of deposited Pt charge density (Q_{Pt}) was calculated by integrating the current density during deposition (Fig. S2a). It was noted that Q_{Pt} varies linearly, to a very good extent, with the deposition time, taking values from nearly 20 mC/cm^2 to above 100 mC/cm^2 (Fig. S2b).

Representative FE-SEM images showing the surface morphology of the as-prepared Pt films at various deposition times are illustrated in Fig. 1. Similarly, the corresponding FE-SEM images of the selenized Pt films are presented in Fig. 2. We observe that the Pt-50 and Pt-100 films consist of sparsely dispersed and nearly spherical Pt nanoparticles (NPs) (Fig. 1a-d). Their size distribution and the coverage fraction of the FTO substrate were determined using an image processing analysis software (Gwyddion) and the derived results are shown in Figs. S3 and S4.

For the Pt-50 film, NPs with sizes range from 100 to nearly 300 nm, with most of them having sizes in the range of 150-250 nm (Fig. S3a). For longer deposition times, or equally for a larger Q_{Pt}, we observe a skew-symmetric size distribution which is reminiscent of a log-normal distribution (Fig. S3b). The main peak of the distribution is in the range 50-150 nm, while the tail extends up to 350 nm. Similar trends were also observed by Zhang *et al*. [52], who used a potentiostatic method for realizing one-step electrodeposition of Pt nanoflowers.

Extending further the deposition time, i.e., for the Pt-200 and Pt-400 films, the previously observed Pt NPs with sizes above 100 nm have been evolved now to superstructures with shapes resembling nanoflowers. However, small NPs with sizes lower than 50 nm are dispersed in the space between the nanoflowers (Fig. 1e-h and Fig. S3c-d). The observed morphology evolution from nearly spherical to flower-like structures is expected to enhance further the electrocatalytically active surface area. Evidently, the coverage fraction of the FTO substrate increase in a sublinear way vs. the electrodeposition time, as shown in Fig. S4.

Selenization engenders enhanced surface roughness of the Pt nanostructures (NPs and nanoflowers) in all films prepared by various deposition times, as shown in Fig. 2. Especially, as deposition time increases, vertical growth of $PtSe_2$ layers is more probable due to the increased thickness of the predeposited Pt films, as stated in [43,53].

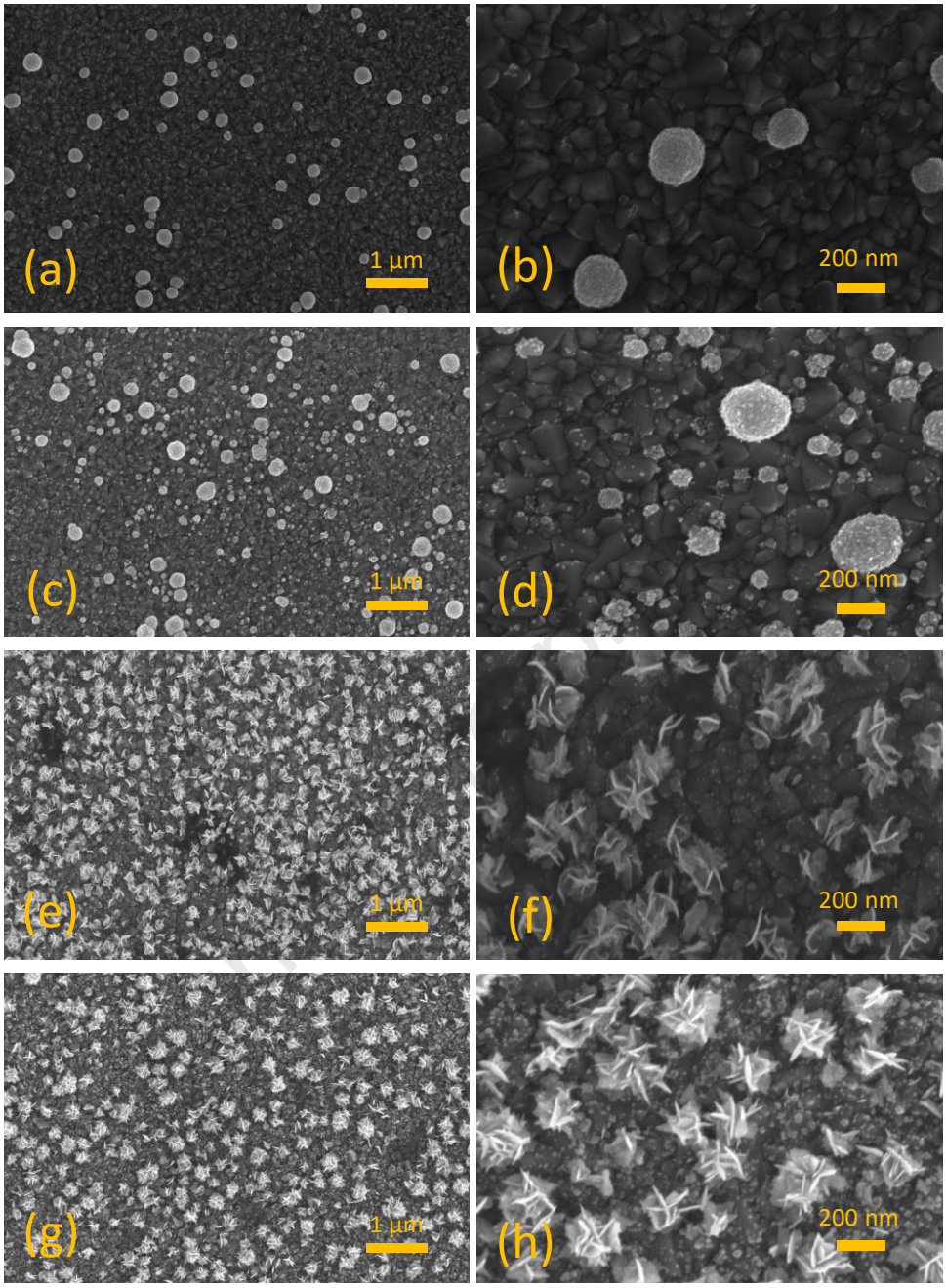

Fig. 1: FE-SEM images of electrodeposited Pt films grown on a FTO substrate at different electrodeposition times: (a, b) 50s, (c, d) 100s, (e, f) 200s and (g, h) 400s. Left column: low magnification; right column: high magnification.

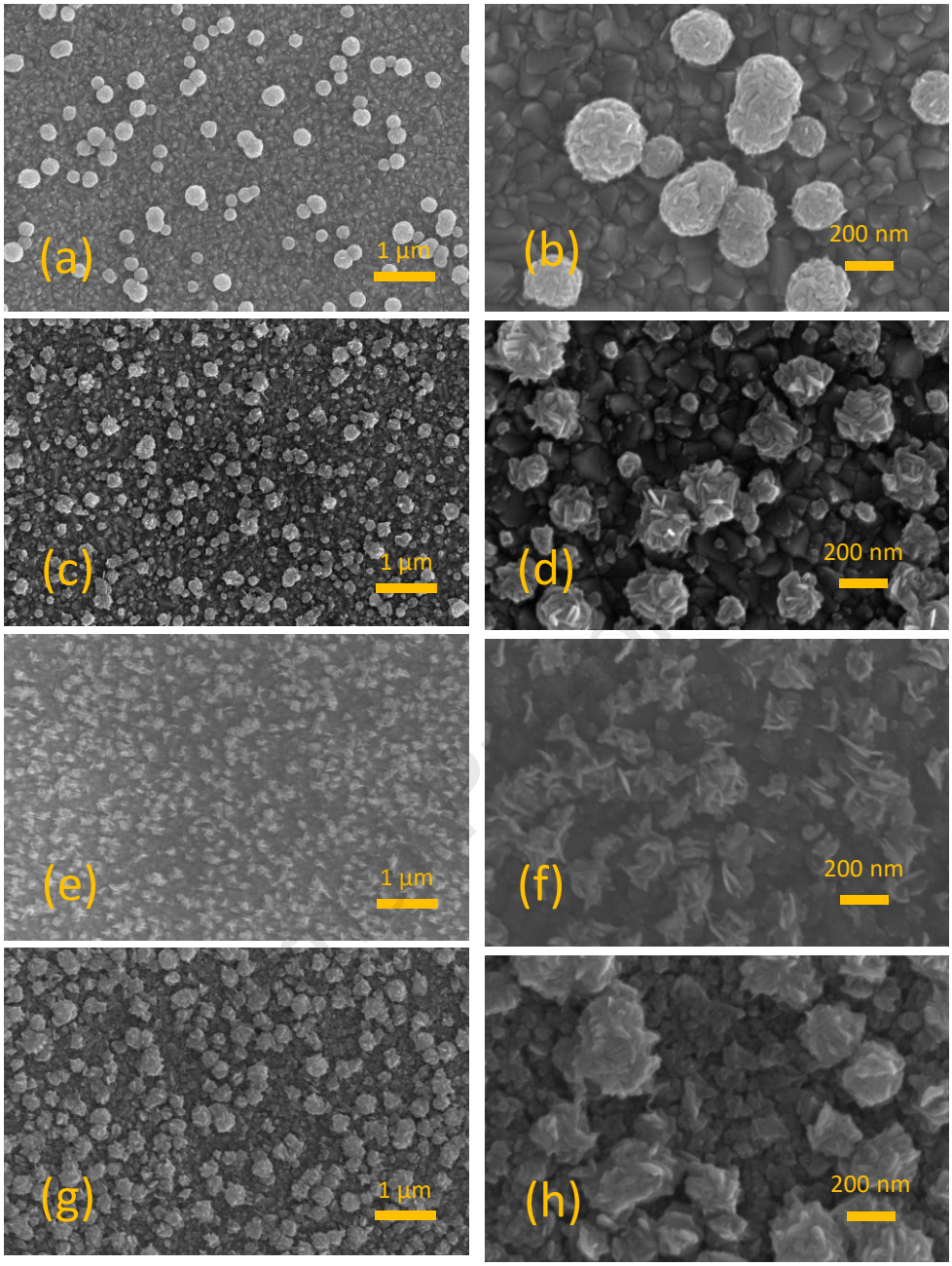

Fig. 2: FE-SEM images of electrodeposited Pt films on an FTO substrate, after selenization, for different electrodeposition times: (a, b) 50s, (c, d) 100s, (e, f) 200s and (g, h) 400s. Left column: low magnification; right column: high magnification.

3.2 Analysis of XPS and Raman spectra

Figure 3 shows the combined XPS Pt4f and Se3d spectral window of sPt-50 and sPt-200 films, respectively. For both spectra, the Pt4f band appears as a doublet, which is analysed into two components assigned to the following chemical states: (i) metallic platinum Pt^0 ($Pt4f_{7/2}$ = 71.2 eV) and platinum bonded to Se forming $PtSe_2$ ($Pt4f_{7/2}$ = 73.0 eV). The data reveal that there is an unreacted fraction of the pre-deposited Pt film on the FTO surface. On the other hand, the Se3d

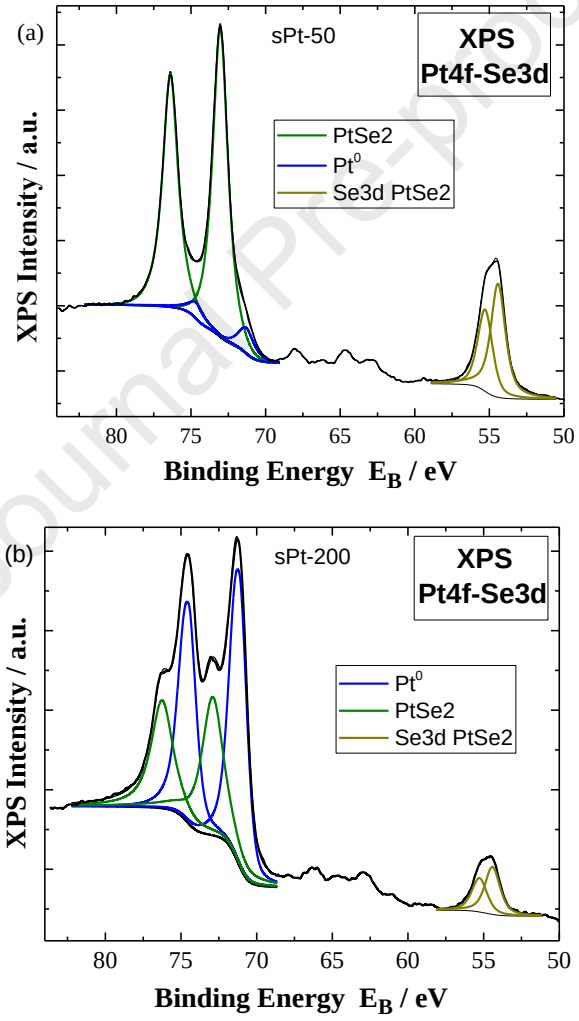

Fig. 3: Pt4f-Se3d XPS spectral window showing the deconvoluted Pt4f and Se3d core level peaks of sPt-50 (a) and sPt-200 (b) films.

doublet consists of one component assigned to Se atoms fully bonded to Pt, i.e. $PtSe_2$ ($Se3d_{3/2}$ = 54.6 eV) [54]. The percentage concentrations of the Pt and Se are calculated using the integrated peak areas of Pt4f and Se3d; the results are shown in Table 1. The above analysis shows that for the current conditions of selenization of the Pt-50 films, i.e. 430 ^{o}C for 90 min, there is a minor fraction of the Pt metal, of about 12 %, which remains unreacted. Keeping the same selenization conditions the same for all films, it is obvious that for the films with higher Pt loading via electrodeposition, an increased fraction of Pt metal will remain unreacted. Indeed, the Pt^0 fraction for the Pt-200 film amounts to ~62%. Based on thermodynamic arguments, we expect that selenization takes place starting from the outer surface of the NPs and the flower-like structures and a schematic for the formation mechanism appears in Fig. S5. Therefore, it is expected that the $PtSe_2$ component appears as a skin covering conformally the Pt particles, leaving the unreacted Pt^0 component in deeper levels below the electrochemically active surface. In this context, it can be safely concluded that the Pt^0 component, does not come into contact with the electrolyte and hence, the unreacted Pt fraction, does not contribute to the electrochemical effects studied here.

Table 1: Pt:Se relative atomic ratios, Se component concentration of sPt-50 and sPt-200 films.

Species / Sample	Pt:Se atomic ratio	Se component concentration	Pt component concentration
sPt-50	1:2.07	100% $PtSe_2$	88% $PtSe_2$ 12% Pt^0
sPt-200	1:0.59	100% $PtSe_2$	38% $PtSe_2$ 62% Pt^0

Raman scattering was used to study the crystallinity and estimate the thickness of the various selenized films. $PtSe_2$ grows in the 1T octahedral structure and belongs to the D_{3d} point group symmetry. There are two dominant Raman modes denoted by the A_{1g} and E_g symmetries, which are assigned to the out-of-plane and in-plane vibrations of Se atoms, respectively. To examine the homogeneity of the selenized films, several Raman spectra were collected from each one, which exhibited almost identical spectra. Typical Raman spectra for each of the selenized films are presented in Fig. 4. The A_{1g} peak wavenumber varies in the range 205–207 cm^{-1} among the various samples. Similarly, the wavenumber of the E_g peak lies within the range 175–178 cm^{-1}. These values agree with the literature data provided by various groups. A much weaker band appears

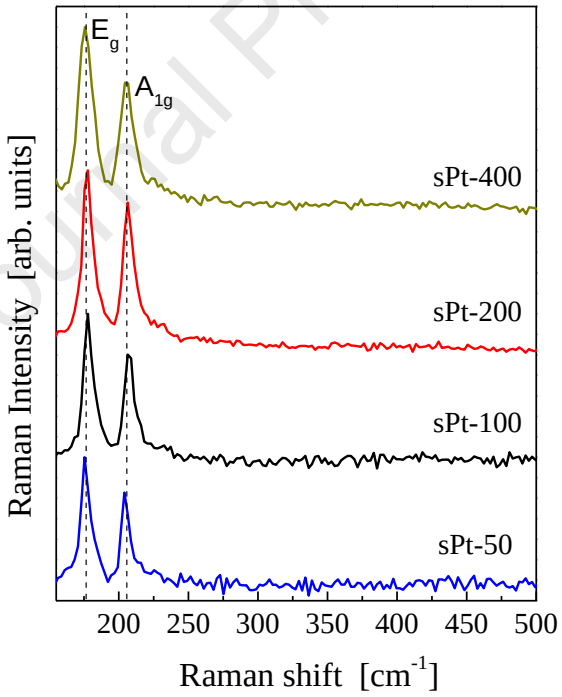

Fig. 4: Raman spectra of selenized Pt films prepared by different deposition times. The Raman bands are assigned to the $PtSe_2$ bands with symmetries A_{1g} and E_g.

near 230 cm^{-1}, which is assigned to an overlap between the A_{2u} and E_u modes, and becomes more intense when the $PtSe_2$ film thickness is reduced to 1-2 monolayers as shown by O' Brien *et al*. [55]. Further, in that work [55] the authors suggested a correlation between the features of the Raman peaks and the number of $PtSe_2$ monolayers. The E_{2g} peak shifts from 174 to 182 cm^{-1} when the film thickness changes from 5 to 0.5 nm. At the same time, the band intensity ratio A_{1g} / E_g decreases from ~1.1 to ~0.3 upon decreasing the film thickness from 5 to 0.5 nm. The current data show that this band intensity ratio varies between 0.6 and 0.8. Based on this finding and considering the variation in the wavenumber of E_g band among the various films, it is concluded that there is a distribution in the thickness of the $PtSe_2$ films ranging from 1 to 5 nm. This is not an unexpected finding because XPS analysis has shown the existence of a rather thin layer of $PtSe_2$, which permits a strong signal to be recorded from the underneath Pt^0 component. The partial selenization of particles with broad size distribution can justify the presence of a variety of $PtSe_2$ particles ranging from few-layer to several (more than 10) layers thick.

3.3 Electrochemical properties of Pt and $PtSe_2$ electrodes

Typical CVs of the as-prepared Pt electrodes at various deposition times, before and after selenization, appear in Fig.5a and Fig. 5b, respectively. As expected, two anodic (Peak I and Peak II) and two cathodic current peaks (Peak I′and Peak II′) are observed, that correspond to the following chemical reactions [56]:

$$\textit{Peak I:}\ 3I^- \rightarrow I_3^- + 2e^-$$

$$\textit{Peak II:}\ 2I_3^- \rightarrow 3I_2 + 2e^-$$

$$\textit{Peak II′:}\ 3I_2 + 2e^- \rightarrow 2I_3^-$$

$$\textit{Peak I′:}\ I_3^- + 2e^- \rightarrow 3I^-$$

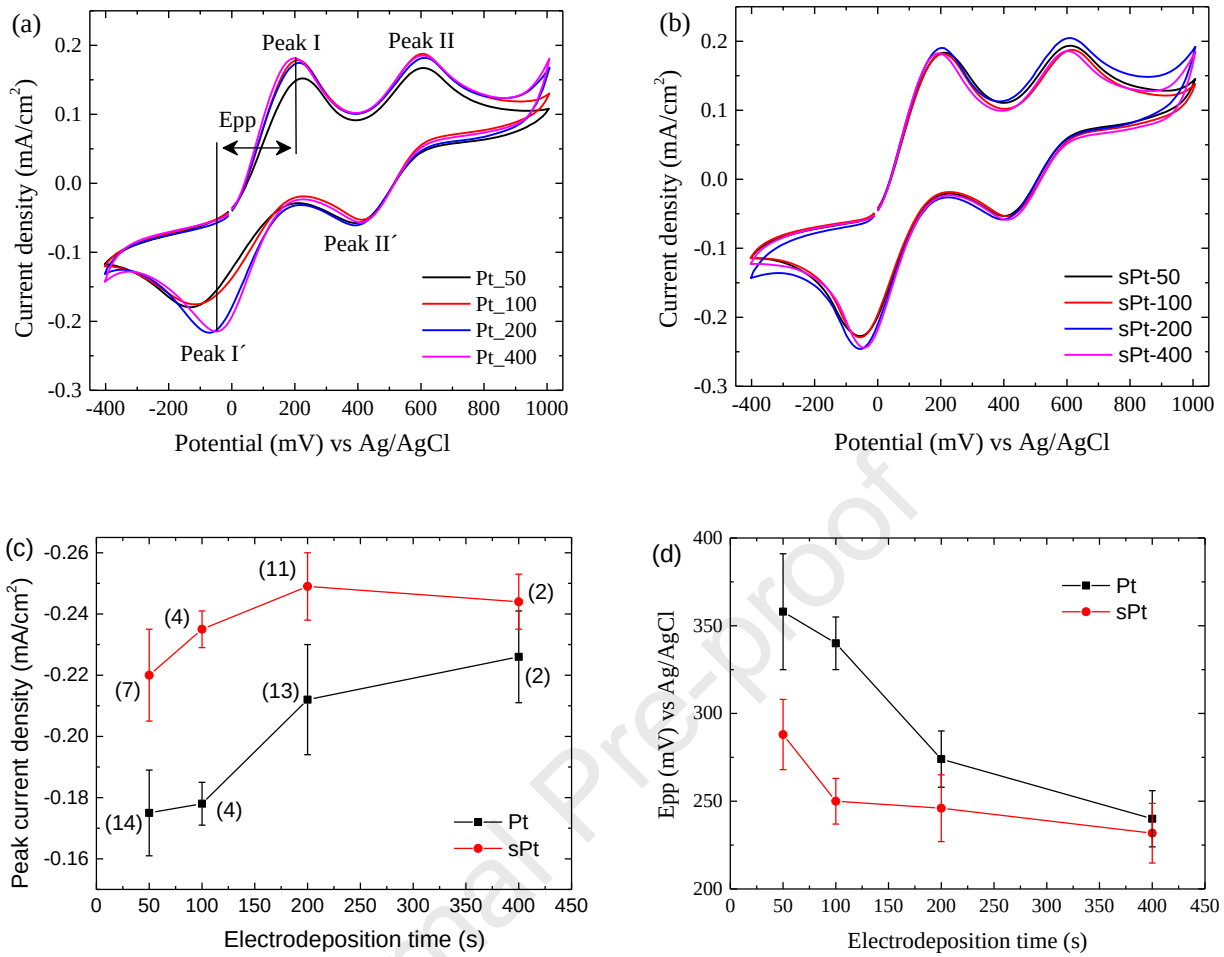

Fig. 5: Typical CVs of the as-prepared Pt electrodes at various deposition times, before (a) and after selenization (b) (scan rate: 20 mV/s). Peak current density (Jpeak) for triiodide reduction (c) and peak-to-peak potential values (d) at various deposition times.

The variation of the peak current density (J_{peak}) for the reduction of triiodide ions (Peak I´) with deposition time, before and after selenization, appears in Fig. 5c, where the numbers in parentheses show the samples used for estimating the average values and the error bars. We observe that in the case of bare Pt electrodes, J_{peak} value shows a negligible increment when deposition time was increased from 50 to 100 s, even though Q_{Pt} was increased significantly from 21 to 32 mC/cm^2 (Fig. S2b) leading also to an increment in the coverage fraction of the

FTO substrate (Fig. S4). Therefore, the presence of Pt NPs with size less than 100 nm (Fig. 1c-d and Fig. S3b) does not further improve the electrocatalytic properties of the electrodes and an optimum Pt NP's size is above 150 nm. Similarly, in [12] for thermal evaporated Pt films, the increment of Pt film thickness beyond 10 nm led also to a negligible improvement in J_{peak} value, probably due to the coalescence of particles into a nearly uniform film. In our case, the size of the particles determines the electrocatalytic properties.

When deposition time increases further, i.e. for the Pt-200 electrode, except from the higher Q_{Pt} (65 mC/cm^2) and coverage fraction (Fig. S2b and S4), the morphology of Pt also changed from nearly spherical to flower-like (Fig. 1e-f). Therefore, extra catalytic active sites are revealed, leading to an enhanced electrochemical active surface area and thus improving significantly the J_{peak} value [52]. However, for the Pt-400 electrode, a further negligible increment in J_{peak} value was observed, even though Q_{Pt} was nearly doubled (116 mC/cm^2) (Fig. S2b). Due to the higher amount of Q_{Pt}, a larger number of NPs fills the space between the nanoflowers, having sizes less than 100 nm (Fig. 1e-h). As a result, their contribution to the electrocatalytic performance of the electrodes is limited. Therefore, the increment in the J_{peak} value doesn't follow the increment in Q_{Pt} and in the surface coverage fraction.

The same behaviour was observed after selenization, even though the variation in J_{peak} with the electrodeposition time was not as intense as in the case of bare Pt electrodes. However, the J_{peak} value of sPt electrodes was increased compared with equivalent bare Pt electrodes, revealing an improved number of catalytic actives sites for I_3^- reduction (Fig. 5c). As depicted from the SEM images (Fig. 2), after selenization, the surface roughness increases, also due to the vertical growth of the $PtSe_2$ layers, leading to an improved electrocatalytic active surface area with plenty of edge sites.

The peak-to-peak potential (E_{pp}) values between Peak I and Peak I′ appears in Fig. 5d. High values indicating a lower reaction rate of the corresponding redox reactions, were observed for Pt-50 electrodes initially, followed by a steep reduction in the case of Pt-200 electrodes. However, an improved reaction rate and a reduced charge transfer resistance (R_{CT}) at the interface are expected, regardless of the deposition time, for sPt electrodes compared with equivalent bare Pt electrodes, resulting from the lower values of E_{pp} (Fig. 5d).

To estimate the values of the R_{CT} for Pt-200 and sPt-200 electrodes, Tafel and EIS analysis were performed. In Tafel polarization curves (Fig. 6a), the intercept with the y-axis of the line resulting from the linear regression analysis in the Tafel zone (200 mV< V <400 mV) of the cathodic or the anodic branch is the exchange current density J_o. R_{CT} can be calculated using Eq. 1 [28,57,58]:

$$R_{CT} = \frac{RT}{nF\,J_o} \qquad \text{(Eq. 1)}$$

where R is the gas constant, T the temperature, F the Faraday's constant and n the number of electrons involved in I_3^- reduction reaction (n=2).

A significant increment in the value of J_o (Table 2), leading to a lower value of R_{CT} (Eq. 1), was achieved for a sPt-200 electrode compared with a Pt-200 electrode, implying a better electrocatalytic activity and a more facile electron transfer process at the CE/electrolyte interface, in agreement with the CV results (Fig. 5c-d). A high value of J_o or equally a low value of R_{CT} could lead also to a high value of short circuit current density (J_{sc}) of the resulting DSSCs [26–28]. Moreover, from the Tafel polarization curves (Fig. 6a), the limiting current density (J_{lim}) is found by the intersection of the cathodic branch of the curves with the y-axis and can be expressed by Eq. 2 [25,28,59]:

$$J_{\lim} = \frac{2nq_e DcN_A}{l} \qquad \text{(Eq. 2)}$$

where N_A is the Avogadro constant, *l* is the spacer thickness, D is the diffusion constant, n is the number of electrons involved in I_3^- reduction reaction (n=2), q_e is the elementary charge and c is the concentration of I_3^- ions. Therefore, a high value of J_{lim} in the case of sPt-200 electrode (Table 2) corresponds to a high value of the diffusion coefficient. Nevertheless, D was estimated also from cyclic voltammetry using different scan rates, as shown below.

Nyquist plots of symmetrical cells with Pt-200 and sPt-200 electrodes are shown in Fig. 6b and the equivalent circuit used for fitting the EIS spectra is shown in the inset of Fig. 6b. Two semicircles, one at the high frequency region (left) and one at the low frequency region (right), are obvious. The intercept with the real axis (Z´) at the high frequency region represents the series or ohmic resistance (R_s). Its value is determined both by the resistance of the FTO substrate and the contact resistance, and as expected is the same for both Pt-200 and sPt-200 electrodes (Table 3). From the diameter of the left semicircle in the high-frequency region, the values of the R_{CT} at the CE/electrolyte interface were estimated. The R_{CT} decreases from 0.259 Ω cm^2 to 0.132 Ω cm^2, in agreement with the results from the Tafel analysis (Table 2). A decreased value of R_{CT} is essential for achieving a high fill factor (FF) in the resulting DSSCs since it affects their internal series resistance (Rs) [27,57]. Moreover, the higher value of the capacitance (C) achieved for sPt-200 electrode shows a large contact surface area between the CE and the electrolyte (Table 2) [33,60], as expected from the higher J_{peak} values (Fig. 5c).

Table 2: Parameters obtained by Tafel and EIS analysis.

Sample	J_o (A/cm^2)	$R_{CT\text{-}Tafel}$ (Ω cm^2)	J_{lim} (A/cm^2)	Rs (Ω cm^2)	$R_{CT\text{-}EIS}$ (Ω cm^2)	C (μF)
Pt-200	0.00505	2.56	0.044	12.9	0.259	33.4
sPt-200	0.00834	1.55	0.056	13.0	0.132	96.9

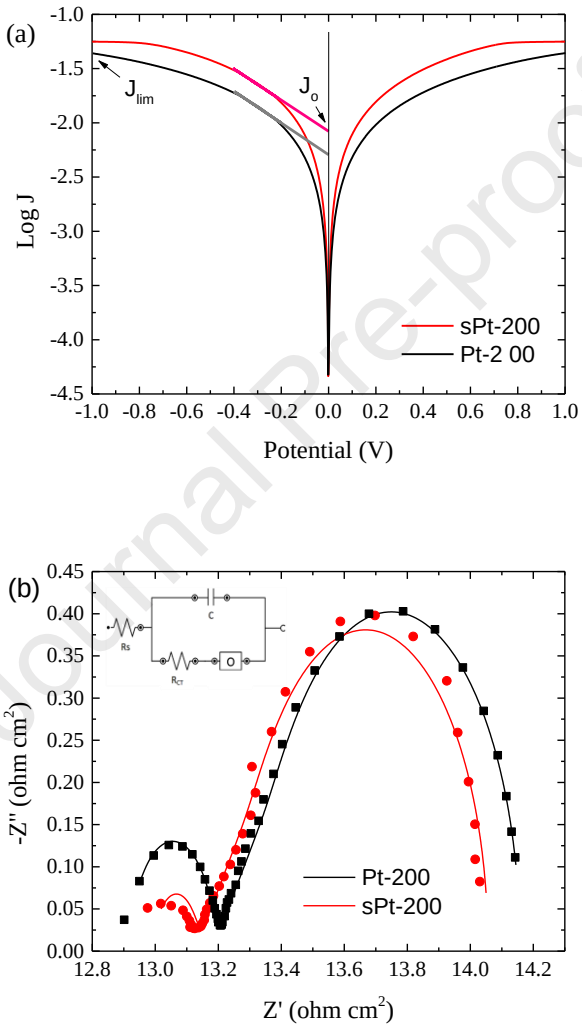

Fig. 6: (a) Tafel polarization curves and (b) Nyquist plots of Pt-200 and sPt-200 electrodes (inset: equivalent circuit used for fitting the EIS spectra, where Rs is the series or ohmic resistance, R_{CT} the charge transfer resistance at the CE/electrolyte interface, C the total capacitance and O the diffusion impedance of I^-/I_3^- redox couple in the electrolyte). The geometric area has been considered.

From the above, the improved electrocatalytic properties of sPt electrodes compared with equivalent bare Pt electrodes has been verified by different techniques. Besides this, the CV experiments have revealed that the sPt-50 electrodes have a comparable performance with the Pt-200 electrodes (Fig. 5c-d), even though Pt loading is three times smaller (Fig. S2b). Therefore, then we have focused on the properties of Pt-50, Pt-200 electrodes and their selenized counterparts, i.e., sPt-50 and sPt-200, before using them as CEs in DSSCs.

The diffusion coefficient of triiodide ions was calculated for Pt-50 and Pt-200 electrodes and their stability under successive cycling was evaluated, along with their selenized counterparts, i.e., sPt-50 and sPt-200 electrodes. Therefore, CVs for Pt-50 and Pt-200 electrodes were recorded at different scan rates ranging from 5 to 60 mV/s and the results are shown in Fig. 7a and 7b, respectively. Both peak current densities (Peak I and I′) increase linearly with the square root of the scan rate (Fig. 7c), according to the Randles-Sevcik equation (Eq. 3), which indicates that the mass transport can be approximately described in diffusional terms. Moreover, from the peak current density (J_{peak}) for Peak I′, the diffusion coefficient of I_3^- ions was calculated with the use of the Randles-Sevcik equation (Eq. 3):

$$I_{peak} = \left(2.69 \times 10^5\right) \cdot n^{3/2} \cdot A \cdot D_a^{1/2} \cdot C_0^* \cdot v^{1/2} \qquad \text{(Eq. 3)}$$

where I_p is the peak current in Amperes, A is the electrode surface, n is the number of electrons involved in the reaction (n = 2), D_α is the diffusion coefficient, C_o^* is the bulk concentration of the I_3^- ions, and ν is the scan rate. The calculated values are shown in Fig. 7c, and as expected a higher value is achieved for Pt-200 electrode, due to the larger availability of catalytic active sites provided by the flower-like nanostructures and the improved reaction rate.

Moreover, to evaluate their stability upon cycling, up to 100 successive cycles were performed. No significant changes were observed for both Pt-50 and Pt-200 electrodes (Fig. 7d

and 7e). More specifically, the J_{peak} value for triiodide reduction (Peak I′), after an initial increment, attained a stable value both for Pt-50 and Pt-200 electrodes (Fig. 7f).

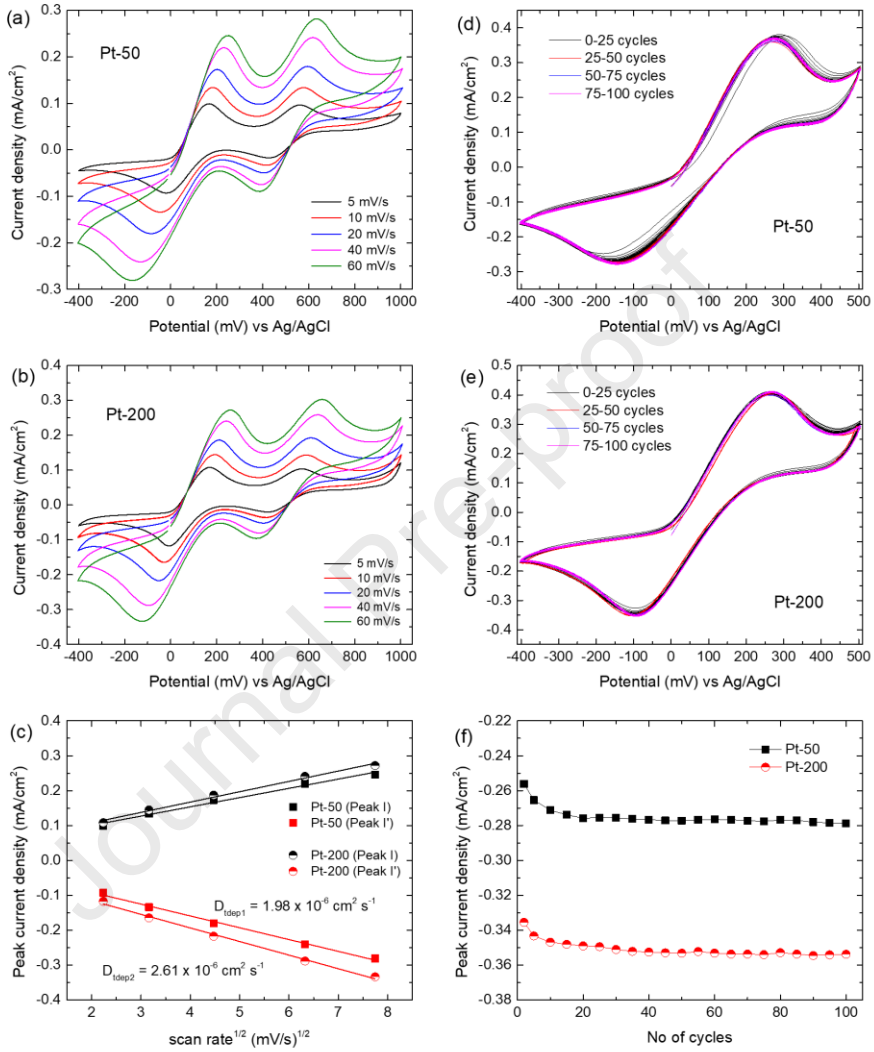

Fig. 7: Typical CVs of (a) Pt-50 and (b) Pt-200 electrodes at different scan rates, (c) Variation of peak current densities against the square root of the scan rate, Plot of 100 consecutive scans of (d) Pt-50 and (e) Pt-200 electrodes (scan rate: 50 mV/s), (f) Variation of peak current density for triiodide reduction with the number of cycles.

In Fig.8a and 8b appear CVs recorded at different scan rates (from 5 mV/s to 60 mV/s) for sPt-50 and sPt-200 electrodes, respectively. As previously, both peak current densities (Peak I and I′) increase linearly with the square root of the scan rate (Fig. 8c). Diffusion coefficients of $2.41x10^{-6}$ cm^2 s^{-1} and $3.53x10^{-6}$ cm^2 s^{-1} were calculated for sPt-50 and sPt-200 electrodes, showing an improvement of nearly 22 % and 35 %, compared with Pt-50 and Pt-200 electrodes, respectively. However, after examining their stability upon cycling (Fig. 8d and 8e), the J_{peak} value for I_3^- reduction of the sPt-200 electrode was reduced by nearly 5%, whereas the sPt-50 electrode retains the 97% of the initial value of J_{peak}. A similar percentage was achieved in [30] for a $Co_{20.85}Se_{79.15}$ CE.

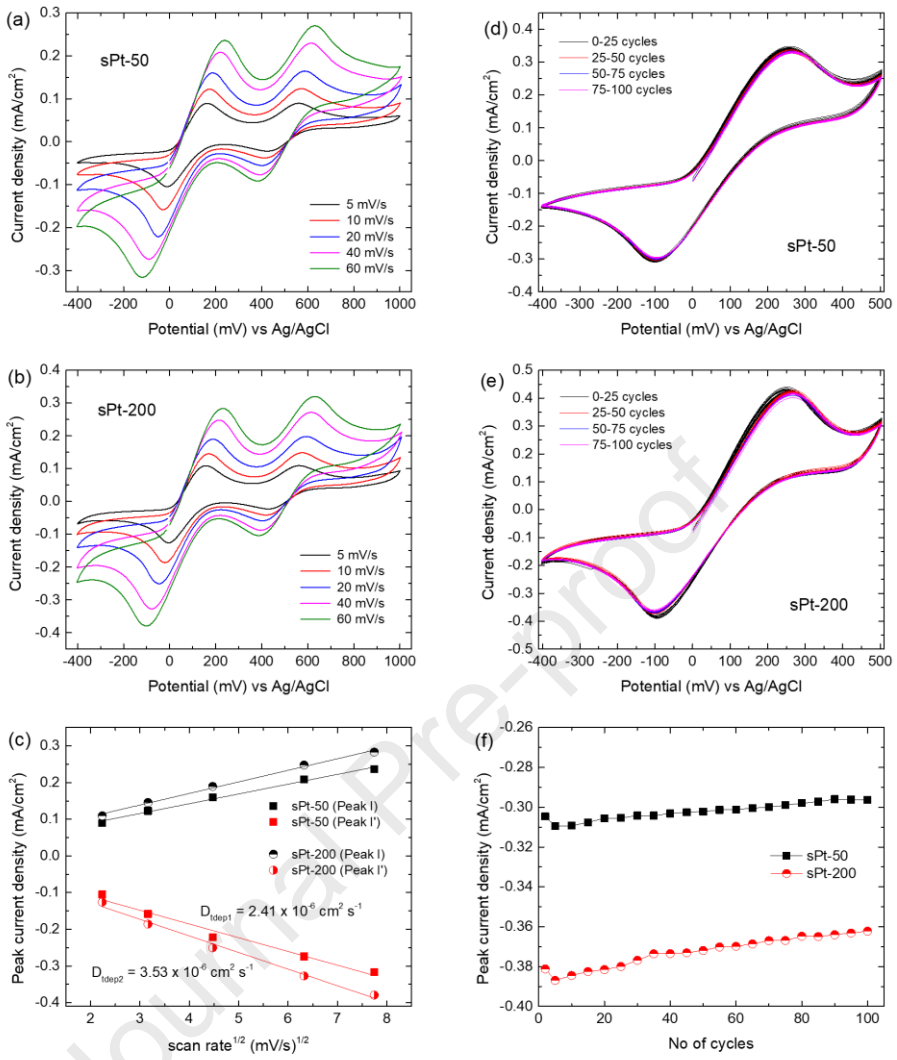

Fig. 8: Typical CVs of (a) sPt-50 and (b) sPt-200 at different scan rates, (c) Variation of peak current densities against the square root of the scan rate, Plot of 100 consecutive scans of (d) sPt-50 and (e) sPt-200 electrodes (scan rate: 50 mV/s), (f) Variation of peak current density for triiodide reduction with the number of cycles.

3.4 Performance of Pt and $PtSe_2$ counter electrodes in DSSCs

As-prepared Pt-50 and Pt-200 electrodes and the corresponding sPt electrodes, i.e., sPt-50 and sPt-200, were used as counter electrodes (CEs) in DSSCs. Typical J-V curves for bare Pt and

sPt CEs are shown in Fig. 9a and Fig. 9b, respectively, and their photovoltaic properties, derived from measuring each time the J-V curves of 3 identical solar cells, are shown in Table 3. The series resistance R_s was also calculated, using Eq. 4, and plotting the variables $-dV/dJ$ vs $(J_{sc}-J)^{-1}$.

$$-\frac{dV}{dJ}=\frac{Ak_BT}{e}\cdot\left(J_{sc}-J\right)^{-1}+R_s \qquad \text{(Eq. 4)}$$

where A is the diode ideality factor, k_B is the Boltzmann constant, T is the absolute temperature, e is the elementary charge and R_s is the series resistance. After performing a linear regression analysis, the value of R_s was calculated from the intercept with the y-axis (Fig. 9c) and the results are shown in Table 3 [61].

A significant improvement in J_{sc} and a small increase in FF were observed for devices with Pt-200 CEs compared with Pt-50 CEs, causing an increase in PCE by nearly 20%, from 7.7% to 9.18% (Fig. 9a and Table 3), in agreement with the variation in their electrocatalytic properties. More specifically, the increment of the number of the catalytic active sites with Pt deposition time results in a subsequent increment not only to J_{peak} values in CVs (Fig. 5c) but also to J_{sc} from 15.8 mA/cm^2 to 18.86 mA/cm^2, as also observed in [21]. Moreover, the reduction in the series resistance R_s (Table 3) indicates a decreased value of the charge transfer resistance at the CE/electrolyte interface, as expected also from the variation of the Epp values (Fig. 5d), improving FF [12,62].

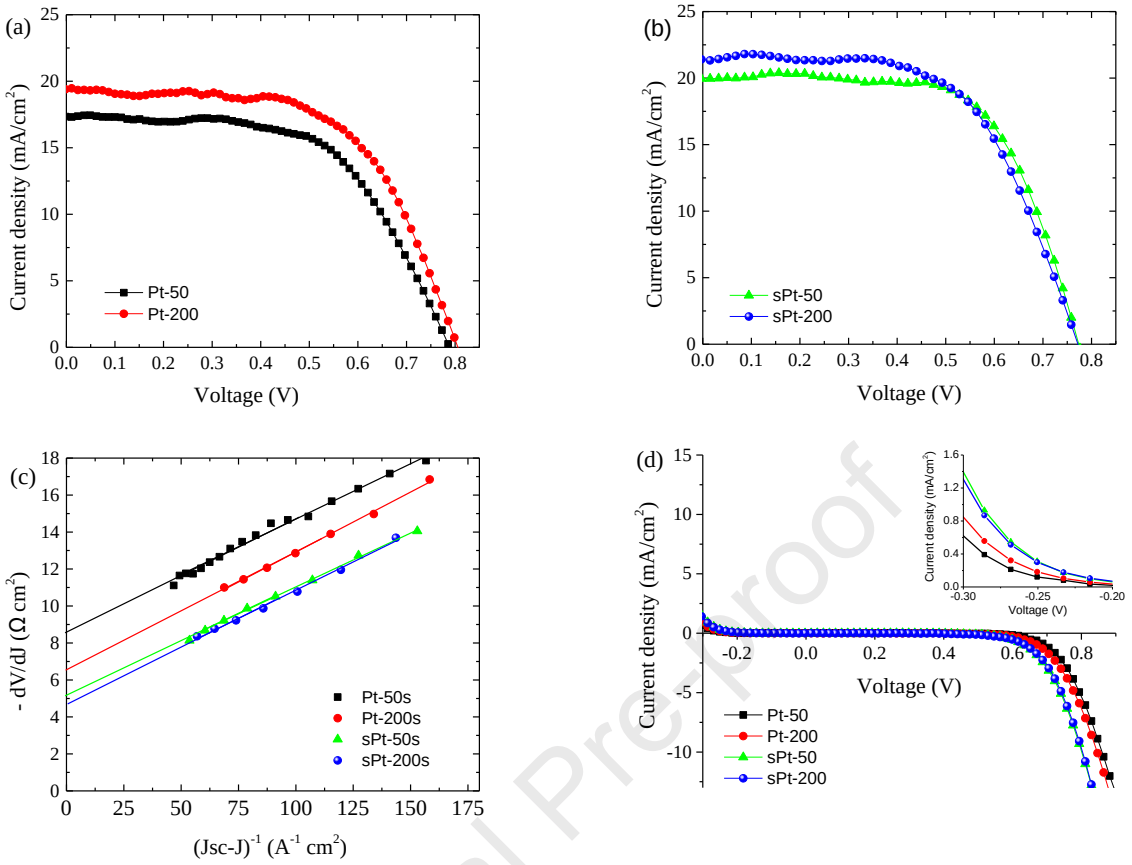

Fig. 9: J-V curves of best performing DSSCs with (a) Pt CEs and (b) sPt CEs, (c) typical plots of $-dV/dJ$ vs $(J_{sc}-J)^{-1}$ for the determination of the series resistance, (d) J-V curves under dark conditions

In the case of sPt CEs, the increment of the electrodeposition time had a minor effect on the performance of the resulting DSSCs (Table 3 and Fig. 9b), where all the photovoltaic parameters, including PCE, deviate within the experimental error. More importantly, devices with sPt-50 and sPt-200 CEs outperform devices with Pt-50 and Pt-200 CEs (Table 3), since the PCE was increased from 7.7% and 9.18% to 9.5% and 9.62%, respectively, while the performance of the devices with sPt-50 CEs is slightly better with that of Pt-200 CEs, even though the later had three times more loading of the Pt metal. The improved performance can be attributed to the higher number of catalytic actives sites for I_3^- reduction and their higher diffusion coefficient, leading to an increment in short circuit current density, while the reduced

value of the R_{CT} at the CE/electrolyte interface leads to a decreased value of Rs, improving FF. Due to the better electrocatalytic properties, a higher current density was measured after applying a reverse bias potential up to –0.3 V under dark conditions (Fig. 9d). The reverse bias potential was kept lower than the value of –0.3 V to avoid degradation of the electrolyte [63]. In this case, electrons flow as under normal operation conditions upon illumination, meaning that triiodide reduction takes place at the CE [64]. Therefore, a higher current density corresponds to a more efficient I_3^- reduction at the CE. Finally, a more facile electron transfer from the CE to the electrolyte is favored in the case of sPt electrodes due to the lower value of the work function (4.8 eV) compared to bare Pt electrodes (5.1 eV) [65,66]. Finally, the stability of the devices a few days after their fabrication doesn't depend on the CE material (Fig. S6).

Table 3: Characteristic photovoltaic properties of DSSCs prepared with bare Pt and sPt CEs

Counter electrode	**Nr of samples**	**V_{oc} (V)**	**J_{sc} (mA/cm^2)**	**FF**	**PCE (%)**	**R_s (Ω cm^2)**	**G_T (W/m2)***
Pt-50	3	0.793 ± 0.007	15.8 ± 1.4	0.613 ± 0.023	7.70 ± 0.19	7.3 ± 1.2	997 ± 40
sPt-50	3	0.779 ± 0.01	18.3 ± 2.1	0.635 ± 0.014	9.5 ± 1.2	5.9 ± 0.9	952 ± 30
Pt-200	3	0.792 ± 0.022	18.86 ± 0.50	0.628 ± 0.034	9.18 ± 0.21	5.8 ± 0.8	1022 ± 40
sPt-200	3	0.773 ± 0.010	19.1 ± 2.0	0.646 ± 0.008	9.62 ± 0.70	5.3 ± 1.3	991 ± 10

*: as measured before each measurement, using a calibrated photodiode

4. Conclusions

In summary, we have investigated the use of Pt and $PtSe_2$ films of varying loading as CEs in DSSCs. Pt films were electrodeposited on FTO substrates for various deposition times. It was found out that the deposition time affects the morphology of the deposited Pt nanostructures and as a result their electrocatalytic properties. Growth of $PtSe_2$ layers, ranging from a few-layers to several, with good homogeneity and conformal coverage of the Pt surface, took place by selenization at a low temperature. An enhanced surface roughness was observed after the growth of $PtSe_2$ layers, and a more facile electron transfer was achieved, leading to an improved electrocatalytic performance compared with bare Pt electrodes with the corresponding loading. Moreover, the performance of $PtSe_2$ CEs exhibits weaker dependence on Pt loading, than the bare Pt CEs. As a result, devices with $PtSe_2$ CEs exhibited superior PCE in relation to the bare Pt CEs with lower Pt loading.

In conclusion, we have proposed a $PtSe_2$-based CE for DSSCs as an alternative solution to achieve similar or higher PCE than that offered by bare Pt CEs, using however, much lower Pt loading. The overall process is simple and scalable, as it is based on short time electrodeposition and low-temperature selenization of the Pt films.

Acknowledgements

G.S. acknowledge the financial support by Greece and the European Union (European Social Fund- ESF) through the Operational Programme «Human Resources Development, Education and Lifelong Learning» in the context of the project “Reinforcement of Postdoctoral Researchers - 2nd Cycle” (MIS-5033021), implemented by the State Scholarships Foundation (IKY). K.B. and S.N.Y. acknowledge support by the European Union’s H2020 research and innovation programme under the Marie Skłodowska-Curie grant agreement N. 721642 (SOLUTION).

References

[1] A.B. Muñoz-García, I. Benesperi, G. Boschloo, J.J. Concepcion, J.H. Delcamp, E.A. Gibson, G.J. Meyer, M. Pavone, H. Pettersson, A. Hagfeldt, M. Freitag, Dye-sensitized solar cells strike back, Chem. Soc. Rev. 50 (2021) 12450–12550. doi:10.1039/D0CS01336F.

[2] P. Cheng, G. Li, X. Zhan, Y. Yang, Next-generation organic photovoltaics based on non-fullerene acceptors, Nat. Photonics. 12 (2018) 131–142. doi:10.1038/s41566-018-0104-9.

[3] O. Inganäs, Organic Photovoltaics over Three Decades, Adv. Mater. 30 (2018) 1800388. doi:10.1002/adma.201800388.

[4] P. Roy, N. Kumar Sinha, S. Tiwari, A. Khare, A review on perovskite solar cells: Evolution of architecture, fabrication techniques, commercialization issues and status, Sol. Energy. 198 (2020) 665–688. doi:10.1016/j.solener.2020.01.080.

[5] M. Que, B. Zhang, J. Chen, X. Yin, S. Yun, Carbon-based electrodes for perovskite solar cells, Mater. Adv. 2 (2021) 5560–5579. doi:10.1039/D1MA00352F.

[6] C. Polyzoidis, K. Rogdakis, E. Kymakis, Indoor Perovskite Photovoltaics for the Internet of Things—Challenges and Opportunities toward Market Uptake, Adv. Energy Mater. 11 (2021) 2101854. doi:10.1002/aenm.202101854.

[7] D.A. Chalkias, C. Charalampopoulos, A.K. Andreopoulou, A. Karavioti, E. Stathatos, Spectral engineering of semi-transparent dye-sensitized solar cells using new triphenylamine-based dyes and an iodine-free electrolyte for greenhouse-oriented applications, J. Power Sources. 496 (2021) 229842. doi:10.1016/j.jpowsour.2021.229842.

[8] G. V. Belessiotis, M. Antoniadou, I. Ibrahim, C.S. Karagianni, P. Falaras, Universal electrolyte for DSSC operation under both simulated solar and indoor fluorescent lighting, Mater. Chem. Phys. 277 (2022) 125543. doi:10.1016/j.matchemphys.2021.125543.

[9] S. Yun, A. Hagfeldt, T. Ma, Pt-Free Counter Electrode for Dye-Sensitized Solar Cells with High Efficiency, Adv. Mater. 26 (2014) 6210–6237. doi:10.1002/adma.201402056.

[10] J. Wu, Z. Lan, J. Lin, M. Huang, Y. Huang, L. Fan, G. Luo, Y. Lin, Y. Xie, Y. Wei, Counter electrodes in dye-sensitized solar cells, Chem. Soc. Rev. 46 (2017) 5975–6023. doi:10.1039/C6CS00752J.

[11] I.-C. Chen, Y.-H. Wei, M.-C. Tsai, F.-G. Tseng, S.-Y. Wei, H.-C. Wu, C.-K. Hsieh, High performance dye-sensitized solar cells based on platinum nanoroses counter electrode, Surf. Coatings Technol. 320 (2017) 409–413. doi:10.1016/j.surfcoat.2016.12.008.

[12] G. Syrrokostas, K. Govatsi, G. Leftheriotis, S.N. Yannopoulos, Platinum decorated zinc oxide nanowires as an efficient counter electrode for dye sensitized solar cells, J. Electroanal. Chem. 835 (2019) 86–95. doi:10.1016/j.jelechem.2019.01.013.

[13] G. Syrrokostas, A. Siokou, G. Leftheriotis, P. Yianoulis, Degradation mechanisms of Pt counter electrodes for dye sensitized solar cells, Sol. Energy Mater. Sol. Cells. 103 (2012) 119–127. doi:10.1016/j.solmat.2012.04.021.

[14] S. Yun, P.D. Lund, A. Hinsch, Stability assessment of alternative platinum free counter electrodes for dye-sensitized solar cells, Energy Environ. Sci. 8 (2015) 3495–3514. doi:10.1039/C5EE02446C.

[15] X. Wang, B. Zhao, W. Kan, Y. Xie, K. Pan, Review on Low-Cost Counter Electrode Materials for Dye-Sensitized Solar Cells: Effective Strategy to Improve Photovoltaic

Performance, Adv. Mater. Interfaces. 9 (2022) 2101229. doi:10.1002/admi.202101229.

[16] Y.-J. Huang, P.K. Sahoo, D.-S. Tsai, C.-P. Lee, Recent Advances on Pt-Free Electro-Catalysts for Dye-Sensitized Solar Cells, Molecules. 26 (2021) 5186. doi:10.3390/molecules26175186.

[17] U. Ahmed, M. Alizadeh, N.A. Rahim, S. Shahabuddin, M.S. Ahmed, A.K. Pandey, A comprehensive review on counter electrodes for dye sensitized solar cells: A special focus on Pt-TCO free counter electrodes, Sol. Energy. 174 (2018) 1097–1125. doi:10.1016/J.SOLENER.2018.10.010.

[18] G.R. Li, X.P. Gao, Low-Cost Counter-Electrode Materials for Dye-Sensitized and Perovskite Solar Cells, Adv. Mater. 32 (2020). doi:10.1002/ADMA.201806478.

[19] Z. Jin, M. Zhang, M. Wang, C. Feng, Z.-S. Wang, Metal Selenides as Efficient Counter Electrodes for Dye-Sensitized Solar Cells, Acc. Chem. Res. 50 (2017) 895–904. doi:10.1021/acs.accounts.6b00625.

[20] S.E. Sheela, R. Sekar, D.K. Maurya, M. Paulraj, S. Angaiah, Progress in transition metal chalcogenides-based counter electrode materials for dye-sensitized solar cells, Mater. Sci. Semicond. Process. 156 (2023) 107273. doi:10.1016/J.MSSP.2022.107273.

[21] J. De Peng, Y.T. Wu, M.H. Yeh, F.Y. Kuo, R. Vittal, K.C. Ho, Transparent Cobalt Selenide/Graphene Counter Electrode for Efficient Dye-Sensitized Solar Cells with Co2+/3+-Based Redox Couple, ACS Appl. Mater. Interfaces. 12 (2020) 44597–44607. doi:10.1021/acsami.0c08220.

[22] Y. Duan, Q. Tang, B. He, Z. Zhao, L. Zhu, L. Yu, Bifacial dye-sensitized solar cells with transparent cobalt selenide alloy counter electrodes, J. Power Sources. 284 (2015) 349–

354. doi:10.1016/j.jpowsour.2015.03.045.

[23] Y. Duan, Q. Tang, B. He, R. Li, L. Yu, Transparent nickel selenide alloy counter electrodes for bifacial dye-sensitized solar cells exceeding 10% efficiency, Nanoscale. 6 (2014) 12601–12608. doi:10.1039/C4NR03900A.

[24] G. Syrrokostas, G. Leftheriotis, S.N. Yannopoulos, Lessons learned from 25 years of development of photoelectrochromic devices: A technical review, Renew. Sustain. Energy Rev. 162 (2022) 112462. doi:10.1016/j.rser.2022.112462.

[25] Y. Duan, Q. Tang, J. Liu, B. He, L. Yu, Transparent Metal Selenide Alloy Counter Electrodes for High-Efficiency Bifacial Dye-Sensitized Solar Cells, Angew. Chemie. 126 (2014) 14797–14802. doi:10.1002/ange.201409422.

[26] H. Sun, L. Zhang, Z.-S. Wang, Single-crystal CoSe 2 nanorods as an efficient electrocatalyst for dye-sensitized solar cells, J. Mater. Chem. A. 2 (2014) 16023–16029. doi:10.1039/C4TA02238F.

[27] H. Sun, L. Zhang, G. Zhou, Z.-S. Wang, CoSe Hollow Spheres with Dual Functions for Efficient Dye-Sensitized Solar Cells, Part. Part. Syst. Charact. 33 (2016) 729–733. doi:10.1002/ppsc.201600130.

[28] F. Gong, H. Wang, X. Xu, G. Zhou, Z.-S. Wang, In Situ Growth of Co 0.85 Se and Ni 0.85 Se on Conductive Substrates as High-Performance Counter Electrodes for Dye-Sensitized Solar Cells, J. Am. Chem. Soc. 134 (2012) 10953–10958. doi:10.1021/ja303034w.

[29] Z. Wang, H. Xu, Z. Zhang, X. Zhou, S. Pang, G. Cui, High-Performance Cobalt Selenide and Nickel Selenide Nanocomposite Counter Electrode for Both Iodide/Triiodide and

Cobalt(II/III) Redox Couples in Dye-Sensitized Solar Cells, Chinese J. Chem. 32 (2014) 491–497. doi:10.1002/cjoc.201400003.

[30] W.-W. Liu, W. Jiang, Y.-C. Liu, W.-J. Niu, M.-C. Liu, L.-B. Kong, L. Lee, Z.M. Wang, Y.-L. Chueh, Interface Engineered Binary Platinum Free Alloy-based Counter Electrodes with Improved Performance in Dye-Sensitized Solar Cells, Sci. Rep. 10 (2020) 9157. doi:10.1038/s41598-020-64965-7.

[31] F.Y. Kuo, F.S. Lin, M.H. Yeh, M.S. Fan, L.Y. Hsiao, J.J. Lin, R.J. Jeng, K.C. Ho, Synthesis of Surfactant-Free and Morphology-Controllable Vanadium Diselenide for Efficient Counter Electrodes in Dye-Sensitized Solar Cells, ACS Appl. Mater. Interfaces. 11 (2019) 25090–25099. doi:10.1021/acsami.9b03328.

[32] M.A. Ibrahem, W.-C. Huang, T. Lan, K.M. Boopathi, Y.-C. Hsiao, C.-H. Chen, W. Budiawan, Y.-Y. Chen, C.-S. Chang, L.-J. Li, C.-H. Tsai, C.W. Chu, Controlled mechanical cleavage of bulk niobium diselenide to nanoscaled sheet, rod, and particle structures for Pt-free dye-sensitized solar cells, J. Mater. Chem. A. 2 (2014) 11382–11390. doi:10.1039/C4TA01881H.

[33] J. Guo, S. Liang, Y. Shi, C. Hao, X. Wang, T. Ma, Transition metal selenides as efficient counter-electrode materials for dye-sensitized solar cells, Phys. Chem. Chem. Phys. 17 (2015) 28985–28992. doi:10.1039/C5CP04862A.

[34] L.T.L. Lee, J. He, B. Wang, Y. Ma, K.Y. Wong, Q. Li, X. Xiao, T. Chen, Few-layer MoSe2 possessing high catalytic activity towards iodide/tri-iodide redox shuttles, Sci. Rep. 4 (2014) 4063. doi:10.1038/srep04063.

[35] N.A.Y. Razamin, H.J. Woo, T. Winie, Comparative study of nickel selenide, iron selenide

and platinum on triiodide reduction for dye-sensitized solar cells, Opt. Mater. X. 13 (2022) 100119. doi:10.1016/J.OMX.2021.100119.

[36] H. Wu, Y. Wang, L. Zhang, Z. Chen, C. Wang, S. Fan, Comparison of two nickel selenides materials with different morphologies as counter electrodes in dye-sensitized solar cells, J. Alloys Compd. 745 (2018) 222–227. doi:10.1016/j.jallcom.2018.02.239.

[37] X. Chen, J. Ding, Y. Li, Y. Wu, G. Zhuang, C. Zhang, Z. Zhang, C. Zhu, P. Yang, Size-controllable synthesis of NiCoSe2 microspheres as a counter electrode for dye-sensitized solar cells, RSC Adv. 8 (2018) 26047–26055. doi:10.1039/c8ra04091e.

[38] Y. Gong, Z. Lin, Y.-X. Chen, Q. Khan, C. Wang, B. Zhang, G. Nie, N. Xie, D. Li, Two-Dimensional Platinum Diselenide: Synthesis, Emerging Applications, and Future Challenges, Nano-Micro Lett. 12 (2020) 174. doi:10.1007/s40820-020-00515-0.

[39] C. Yim, K. Lee, N. McEvoy, M. O'Brien, S. Riazimehr, N.C. Berner, C.P. Cullen, J. Kotakoski, J.C. Meyer, M.C. Lemme, G.S. Duesberg, High-Performance Hybrid Electronic Devices from Layered PtSe 2 Films Grown at Low Temperature, ACS Nano. 10 (2016) 9550–9558. doi:10.1021/acsnano.6b04898.

[40] Y. Wang, L. Li, W. Yao, S. Song, J.T. Sun, J. Pan, X. Ren, C. Li, E. Okunishi, Y.-Q. Wang, E. Wang, Y. Shao, Y.Y. Zhang, H. Yang, E.F. Schwier, H. Iwasawa, K. Shimada, M. Taniguchi, Z. Cheng, S. Zhou, S. Du, S.J. Pennycook, S.T. Pantelides, H.-J. Gao, Monolayer PtSe 2 , a New Semiconducting Transition-Metal-Dichalcogenide, Epitaxially Grown by Direct Selenization of Pt, Nano Lett. 15 (2015) 4013–4018. doi:10.1021/acs.nanolett.5b00964.

[41] C. Yim, V. Passi, M.C. Lemme, G.S. Duesberg, C. Ó Coileáin, E. Pallecchi, D. Fadil, N.

McEvoy, Electrical devices from top-down structured platinum diselenide films, Npj 2D Mater. Appl. 2 (2018) 5. doi:10.1038/s41699-018-0051-9.

[42] K. Bhorkar, L. Sygellou, M. Cathelinaud, D. Ren, J.-L. Adam, S.N. Yannopoulos, Band Alignment and Optical Properties of 1D/2D Sb 2 Se 3 /PtSe 2 Heterojunctions, ACS Appl. Electron. Mater. (2022). doi:10.1021/acsaelm.2c00541.

[43] S. Lin, Y. Liu, Z. Hu, W. Lu, C.H. Mak, L. Zeng, J. Zhao, Y. Li, F. Yan, Y.H. Tsang, X. Zhang, S.P. Lau, Tunable active edge sites in PtSe2 films towards hydrogen evolution reaction, Nano Energy. 42 (2017) 26–33. doi:10.1016/j.nanoen.2017.10.038.

[44] H. Huang, X. Fan, D.J. Singh, W. Zheng, Modulation of Hydrogen Evolution Catalytic Activity of Basal Plane in Monolayer Platinum and Palladium Dichalcogenides, ACS Omega. 3 (2018) 10058–10065. doi:10.1021/acsomega.8b01414.

[45] D. Hu, T. Zhao, X. Ping, H. Zheng, L. Xing, X. Liu, J. Zheng, L. Sun, L. Gu, C. Tao, D. Wang, L. Jiao, Unveiling the Layer-Dependent Catalytic Activity of PtSe 2 Atomic Crystals for the Hydrogen Evolution Reaction, Angew. Chemie. 131 (2019) 7051–7055. doi:10.1002/ange.201901612.

[46] J. Shi, Y. Huan, M. Hong, R. Xu, P. Yang, Z. Zhang, X. Zou, Y. Zhang, Chemical Vapor Deposition Grown Large-Scale Atomically Thin Platinum Diselenide with Semimetal–Semiconductor Transition, ACS Nano. 13 (2019) 8442–8451. doi:10.1021/acsnano.9b04312.

[47] Y. He, L. Liu, C. Zhu, S. Guo, P. Golani, B. Koo, P. Tang, Z. Zhao, M. Xu, C. Zhu, P. Yu, X. Zhou, C. Gao, X. Wang, Z. Shi, L. Zheng, J. Yang, B. Shin, J. Arbiol, H. Duan, Y. Du, M. Heggen, R.E. Dunin-Borkowski, W. Guo, Q.J. Wang, Z. Zhang, Z. Liu, Amorphizing

noble metal chalcogenide catalysts at the single-layer limit towards hydrogen production, Nat. Catal. 5 (2022) 212–221. doi:10.1038/s41929-022-00753-y.

[48] X. Chia, A. Adriano, P. Lazar, Z. Sofer, J. Luxa, M. Pumera, Layered Platinum Dichalcogenides (PtS 2 , PtSe 2 , and PtTe 2) Electrocatalysis: Monotonic Dependence on the Chalcogen Size, Adv. Funct. Mater. 26 (2016) 4306–4318. doi:10.1002/adfm.201505402.

[49] G. Syrrokostas, G. Leftheriotis, P. Yianoulis, Pt/Ni counter electrodes with improved stability for dye sensitized solar cells, in: 28th Eur. Photovolt. Sol. Energy Conf., Paris, France, 2013: pp. 2768–2772. doi:10.4229/28thEUPVSEC2013-3DV.2.31.

[50] G. Syrrokostas, G. Leftheriotis, P. Yianoulis, Effect of acidic additives on the structure and performance of TiO2 films prepared by a commercial nanopowder for dye-sensitized solar cells, Renew. Energy. 72 (2014) 164–173. doi:10.1016/j.renene.2014.07.009.

[51] F. Montilla, E. Morallón, I. Duo, C. Comninellis, J.. Vázquez, Platinum particles deposited on synthetic boron-doped diamond surfaces. Application to methanol oxidation, Electrochim. Acta. 48 (2003) 3891–3897. doi:10.1016/S0013-4686(03)00526-7.

[52] H. Zhang, W. Zhou, Y. Du, P. Yang, C. Wang, One-step electrodeposition of platinum nanoflowers and their high efficient catalytic activity for methanol electro-oxidation, Electrochem. Commun. 12 (2010) 882–885. doi:10.1016/j.elecom.2010.04.011.

[53] J.H. Kim, S. Youn, T.W. Go, J. Kim, C. Yoo, M.S. Shawkat, S.S. Han, S. Jeon, Y. Jung, J.Y. Park, W. Lee, Revealing Pt-seed-induced structural effects to tribological/electrical/thermoelectric modulations in two-dimensional PtSe2 using scanning probe microscopy, Nano Energy. 91 (2022) 106693.

doi:10.1016/j.nanoen.2021.106693.

[54] C.-C. Chung, H. Yeh, P.-H. Wu, C.-C. Lin, C.-S. Li, T.-T. Yeh, Y. Chou, C.-Y. Wei, C.-Y. Wen, Y.-C. Chou, C.-W. Luo, C.-I. Wu, M.-Y. Li, L.-J. Li, W.-H. Chang, C.-W. Chen, Atomic-Layer Controlled Interfacial Band Engineering at Two-Dimensional Layered PtSe 2 /Si Heterojunctions for Efficient Photoelectrochemical Hydrogen Production, ACS Nano. 15 (2021) 4627–4635. doi:10.1021/acsnano.0c08970.

[55] M. O'Brien, N. McEvoy, C. Motta, J.-Y. Zheng, N.C. Berner, J. Kotakoski, K. Elibol, T.J. Pennycook, J.C. Meyer, C. Yim, M. Abid, T. Hallam, J.F. Donegan, S. Sanvito, G.S. Duesberg, Raman characterization of platinum diselenide thin films, 2D Mater. 3 (2016) 021004. doi:10.1088/2053-1583/3/2/021004.

[56] G. Syrrokostas, A. Siokou, G. Leftheriotis, P. Yianoulis, Degradation mechanisms of Pt counter electrodes for dye sensitized solar cells, Sol. Energy Mater. Sol. Cells. 103 (2012) 119–127. doi:10.1016/j.solmat.2012.04.021.

[57] R. Kumar, V. Sahajwalla, P. Bhargava, Fabrication of a counter electrode for dye-sensitized solar cells (DSSCs) using a carbon material produced with the organic ligand 2-methyl-8-hydroxyquinolinol (Mq), Nanoscale Adv. 1 (2019) 3192–3199. doi:10.1039/C9NA00206E.

[58] S. Gnanasekar, P. Kollu, S.K. Jeong, A.N. Grace, Pt-free, low-cost and efficient counter electrode with carbon wrapped VO2(M) nanofiber for dye-sensitized solar cells, Sci. Rep. 9 (2019) 5177. doi:10.1038/s41598-019-41693-1.

[59] C. Altinkaya, A. Atli, A. Atilgan, K. Salimi, A. Yildiz, Facile fabrication of low-cost low-temperature carbon-based counter electrode with an outstanding fill factor of 73% for

dye-sensitized solar cells, Int. J. Energy Res. 44 (2020) 3160–3170. doi:10.1002/er.5174.

[60] Z. Lan, J. Wu, J. Lin, M. Huang, Morphology controllable fabrication of Pt counter electrodes for highly efficient dye-sensitized solar cells, J. Mater. Chem. 22 (2012) 3948. doi:10.1039/c2jm15019k.

[61] G. Syrrokostas, G. Leftheriotis, S.N. Yannopoulos, Double-Layered Zirconia Films for Carbon-Based Mesoscopic Perovskite Solar Cells and Photodetectors, J. Nanomater. 2019 (2019) 1–11. doi:10.1155/2019/8348237.

[62] G. Syrrokostas, A. Antonelou, G. Leftheriotis, S.N. Yannopoulos, Electrochemical properties and long-term stability of molybdenum disulfide and platinum counter electrodes for solar cells: A comparative study, Electrochim. Acta. 267 (2018) 110–121. doi:10.1016/j.electacta.2018.02.068.

[63] S. Iwata, S. Shibakawa, N. Imawaka, K. Yoshino, Stability of the current characteristics of dye-sensitized solar cells in the second quadrant of the current–voltage characteristics, Energy Reports. 4 (2018) 8–12. doi:10.1016/j.egyr.2017.10.004.

[64] M. Berginc, M. Topič, U. Opara Krašovec, Recovery of dye-sensitized solar cell's performance by heat treatment, Phys. Chem. Chem. Phys. 16 (2014) 12940–12948. doi:10.1039/C4CP01463D.

[65] Q. Tang, H. Zhang, Y. Uanyuan Meng, B. He, L. Yu, Dissolution Engineering of Platinum Alloy Counter Electrodes in Dye-Sensitized Solar Cells, Angew. Chemie. 127 (2015) 11610–11614. doi:10.1002/ANGE.201505339.

[66] G. Li, X. Gao, Low-Cost Counter-Electrode Materials for Dye-Sensitized and Perovskite Solar Cells, Adv. Mater. 32 (2020) 1806478. doi:10.1002/adma.201806478.

Highlights

- Pt films are prepared by electrodeposition on glass/FTO substrates
- PtSe2 ultrathin layers are synthesized by soft selenization of the Pt films
- Pt and PtSe2 are compared as counter electrodes (CEs) in dye-sensitized solar cells
- DSSCs with Pt CEs exhibit an efficiency up to 9.18%, depending on Pt mass loading
- DSSCs with PtSe2 CEs exhibit an efficiency of 9.5%, with a lower Pt mass loading

Declaration of interests

☐ The authors declare that they have no known competing financial interests or personal relationships that could have appeared to influence the work reported in this paper.

☒ The authors declare the following financial interests/personal relationships which may be considered as potential competing interests:

George Syrrokostas reports was provided by State Scholarships Foundation (IKY). Kapil Bhorkar reports was provided by Marie Curie-Sklodowska grant (SOLUTION). Spyros Yannopoulos reports was provided by Marie Curie-Sklodowska grant (SOLUTION).